J Vis
https://doi.org/10.1007/s12650-026-01115-7

REGULAR PAPER

Lotta Kursula · Felix Kexel · Marko Hoffmann · Niklas-Maximilian Epping · Paul Bubenheim · Koichi Terasaka · Andreas Liese · Michael Schlüter

Experimental studies on microscopic, multiphase transport phenomena: Novel applications of light sheet fluorescence microscopy

Received: 4 September 2025 / Revised: 28 January 2026 / Accepted: 10 February 2026

Abstract Over the past two decades, light sheet fluorescence microscopy has developed to a powerful tool for studies of dynamics in biological systems. In a new development, we apply light sheet fluorescence microscopy as a novel experimental measurement technology within the field of multiphase process engineering and fluid dynamics. The technology enables a number of novel studies of single- and multiphase transport phenomena on a microscopic scale. In the current publication, we introduce the first implementation of light sheet fluorescence microscopy in the field and demonstrate its applicability on one exemplary measurement of diffusive oxygen mass transfer from an oxygen bubble to degassed water. The results prove that such measurements can be conducted with a high spatial resolution with a submicron pixel pitch and enable precise studies on microscopic transport phenomena. Besides measurements of mass transfer, on

L. Kursula (✉) · F. Kexel · M. Hoffmann · M. Schlüter (✉)
Institute of Multiphase Flows, Hamburg University of Technology, Eißendorfer Straße 38, 21073 Hamburg, Hamburg, Germany
E-mail: lotta.kursula@tuhh.de

M. Schlüter
E-mail: michael.schlueter@tuhh.de

F. Kexel
E-mail: felix.kexel@tuhh.de

M. Hoffmann
E-mail: marko.hoffmann@tuhh.de

N.-M. Epping · P. Bubenheim · A. Liese
Institute of Technical Biocatalysis, Hamburg University of Technology, Denickestraße 15, 21073 Hamburg, Hamburg, Germany
E-mail: niklas.epping@tuhh.de

P. Bubenheim
E-mail: paul.bubenheim@tuhh.de

A. Liese
E-mail: liese@tuhh.de

K. Terasaka
Department of Applied Chemistry, Faculty of Science and Technology, Keio University, Hiyoshi 3-14-1, Yokohama, Kanagawa 223-0061, Japan
E-mail: terasaka@applc.keio.ac.jp

Published online: 23 May 2026

which we lay the focus here, light sheet fluorescence microscopy further enables studies of fluid dynamics on a microscopic scale.

Keywords LSFM · SPIM · PLIF · Mass transfer

1 Introduction

Multiphase reaction systems are commonly encountered in, for instance, cell cultivation or biocatalysis, where a dissolved gaseous substrate is needed. If the mass transfer of the gaseous phase to the liquid is slower than its consumption by the reaction, the process is limited by the gas–liquid mass transfer performance (Garcia-Ochoa and Gomez 2009). Therefore, by optimising the gas–liquid mass transfer as well as the transport of the dissolved gas within the liquid phase in such an aerated bioreactor, the efficiency of the process can be improved significantly (Schlüter et al. 2021). To identify potentials for such optimisations, fundamental studies on the governing transport phenomena, namely the gas–liquid mass transfer and fluid dynamics, are needed. As of today, there are many well-established experimental methods to study these phenomena on a macroscopic scale. For instance, laser-induced fluorescence (LIF) or planar laser-induced fluorescence (PLIF) measurements are applied to study the mass transfer from single bubbles and bubble swarms into a liquid bulk (Kursula et al. 2022; Lebrun et al. 2021; Busciglio et al. 2010; Ruiz-Rus et al. 2022; Kexel et al. 2021; Roudet et al. 2017; Francois et al. 2011; Dani et al. 2007; Dai et al. 2025; Alméras et al. 2016). For studies on the relevant fluid dynamics ranging from single bubble dynamics to laboratory-scale bioreactors, methods like particle image velocimetry (PIV) or particle tracking velocimetry (PTV) are applied (Schanz et al. 2016; Filella et al. 2015; Kursula et al. 2022; Alberini et al. 2017; Pavlov et al. 2021; Hofmann et al. 2022). However, studies of transport phenomena on a microscopic scale still have multiple limitations. Often, a trade-off between simultaneous high spatial and temporal resolution has to be taken into account. Furthermore, physical space limitations around the set-ups hinder easy accessibility and, thus, cut down on possibilities for modifications and customisation. In the current work, a novel experimental application of light sheet fluorescence microscopy (LSFM) for studies of local transport phenomena on a microscopic scale is introduced.

In the field of cell biology and neuroscience, LSFM, or selective plane illumination microscopy (SPIM), is already fairly well-established, although further optimisation of the technique is still ongoing (Olarte et al. 2018). In LSFM, a light sheet illuminates a thin plane selectively and a camera captures the fluorescence emission through a second optical path (Olarte et al. 2018; Elisa et al. 2018; Stelzer 2015; et al. 2007). Therefore, the advantages of epi-fluorescence and confocal laser scanning, high spatial resolution and selective plane illumination, are combined and their respective limitations can be overcome (Elisa et al. 2018). The result is a combination of the two main advantages of LSFM: high spatial and temporal resolutions achieved for a simple and non-invasive optical observation of three-dimensional samples (Duocastella et al. 2017; Tomančák and Reynaud 2024). The technology gained large attention in 2004 within the scientific community of biologists when Huisken et al. studied live embryos using LSFM (Huisken et al. 2004). Today, LSFM is considered a powerful tool for biologists for studies on cleared organs and tissue, single cells and their motility, small organisms and their nervous systems as well as many other biological applications (Albert-Smet et al. 2019; Blutke et al. 2020; Elisa et al. 2018; Olarte et al. 2018). The possibility of high temporal resolutions (Elisa et al. 2018) also facilitates studies on the dynamics of biological systems, including lipid hydrodynamics and single-particle tracking (Ritter et al. 2008; Jahl and Parthasarathy 2020). Furthermore, LSFM has been used to study spray dynamics (Berrocal et al. 2018). However, an implementation of the technique in the field of process engineering, multiphase fluid dynamics and gas–liquid mass transfer has not yet been reported to our knowledge. Therefore, we introduce a novel application of LSFM to study local gas–liquid transport phenomena on a microscopic scale.

Although the following details focus on applications within the field of gas–liquid mass transfer, we kindly ask the reader to consider that the set-up is equally suitable for a broad range of studies on the microscopic fluid dynamics of multi- and single-phase systems.

2 Theoretical background

2.1 Common measurement techniques for dissolved gas concentration in multiphase systems

Measurements of local concentration fields of dissolved gas in liquids can deepen our understanding of gas–liquid mass transfer performance and transport through the liquid phase under various conditions. On the one hand, convective systems can be studied for this purpose. In such studies, the thickness of the concentration boundary layer can be obtained from the local concentration fields for varying bubble Reynolds numbers. Furthermore, the evolution of the dissolved gas concentration fields in bubble wakes can be visualised and observed (Francois et al. 2011; Dani et al. 2007; Kursula et al. 2022; Av et al. 2019). Such studies contribute to the understanding of the governing phenomena of mixing within a liquid bulk. On the other hand, more fundamental problems, as solely diffusive processes, can be of interest. In these studies with low dynamics, species-depending variables, like the diffusion or liquid-side mass transfer coefficient, can be obtained (Jimenez et al. 2013). It is, thus, evident that there can be a wide range of experimental objectives and requirements. Depending on the desired experimental focus, it is therefore advantageous if the trade-off between high spatial or high temporal resolution can be eliminated or if the prioritisation is at least flexible. In any case, the resolutions should match the dynamics of the studied system. On a macroscopic scale, this is typically achieved by using light sheets to illuminate selective planes (Rüttinger et al. 2018).

It is therefore clear that studies of mass transfer using a light sheet are not a novelty per se; they offer both high spatial and temporal resolution on a macroscopic scale. Light sheets commonly used within the field of gas–liquid multiphase systems have thicknesses ranging from several hundred micrometres to a few millimetres (Busciglio et al. 2010; Dani et al. 2007; Kováts 2021). However, such thick light sheets are not suitable for studies on a microscopic scale, as shown by Matthes (2021). If the light sheet is too thick, the measurement is more reminiscent of epi-fluorescence, since the two-dimensional section of interest is superimposed with illuminated sections in the front and behind. As a consequence, the local phenomena in the plane of interest cannot be observed due to the overlapping of the illuminated planes. This problem can be overcome by confocal laser scanning microscopy (CLSM), which, however, yields a low temporal resolution (Elisa et al. 2018; Matthes 2021). Therefore, CLSM is limited to studies of stationary systems or systems with low dynamics. LSFM offers a solution to both of the presented challenges, which made it a popular measurement technique for dynamic biological systems in the past two decades (Elisa et al. 2018).

2.2 Introduction to microscopic, diffusive gas–liquid mass transfer

For the interpretation of the measurements of the current work, but primarily for the validation of the applicability of LSFM for the given purpose, a short introduction to microscopic, diffusive gas–liquid mass transfer is given in the following.

In the case of isotropic, pure diffusion, the three-dimensional transport equation in spherical coordinates is simplified to the well-known Fick's second law of diffusion

$$\frac{\partial c_\mathrm{A}}{\partial t} = \frac{1}{r^2} D_\mathrm{A,B} \frac{\partial}{\partial r}\left(r^2 \frac{\partial c_\mathrm{A}}{\partial r}\right), \tag{1}$$

where c_A is the concentration of species A, t is the time, r is the radial coordinate and $D_\mathrm{A,B}$ is the diffusion coefficient of A in B. For the mass transfer of oxygen from a gaseous bubble to water with the initial condition $c(t = 0\,\mathrm{s},\ r) = 0$ and the boundary conditions $c(t,\ r = R) = 0$, R being a faraway radial position, and $c(t,\ r = r_\mathrm{B}) = c^*_{\mathrm{O}_2}$ whilst assuming a constant diffusion coefficient, the solution of Eq. 1 is

$$c_{\mathrm{O}_2}(t, r) = \frac{r_\mathrm{B}}{r} \mathrm{erfc}\left(\frac{r - r_\mathrm{B}}{\sqrt{4tD_{\mathrm{O}_2,\mathrm{H_2O}}}}\right) c^*_{\mathrm{O}_2}, \tag{2}$$

where r_B is the radius of the bubble, $D_{\mathrm{O}_2,\mathrm{H_2O}}$ is the diffusion coefficient of oxygen in water and $c^*_{\mathrm{O}_2}$ is the saturation concentration of oxygen in water.

Strictly speaking, Eqs. 1 and 2 are only valid for binary systems, meaning that no other gaseous species are dissolved in the water. Such multicomponent mass transfer has been studied more excessively for liquid systems, using Maxwell–Stefan diffusion in addition to Fick's law of diffusion (Rehfeldt and Stichlmair 2007; Cussler 2009; Taylor and Krishna 1993), compared to systems where both gases and liquids are

present, as modelled by Fleckenstein and Bothe (2015). In bioprocesses, however, the liquid phase is usually saturated with a range of dissolved gases like CO_2, making those systems at least tertiary and, respectively, complex. Striving for thermodynamic equilibrium, these gases also diffuse from the liquid to the gaseous phase, supposedly influencing the desired mass transfer of the gas to the liquid. This effect, often referred to as counterdiffusion or cross-diffusion, has been quantified on a global scale in (Matthes 2021) and observed in (Karnbach et al. 2016) on a local scale from the shrinking behaviour of a single hydrogen microbubble. Especially on the small scales that we consider in the current work, the effects of counterdiffusion have to be accounted for (Matthes 2021). To circumvent problems arising from such effects, the measurements exhibited in this publication are conducted in physically degassed water, realised by drawing a vacuum. Therefore, Eqs. 1 and 2 can be considered valid for the current case with respect to the number of species in the system.

For small scales and short times where the mass transfer phenomena are expected to be highly transient, the choice of the diffusion coefficient requires careful consideration. To date, the values of diffusion coefficients of dissolved oxygen in water vary strongly in literature. For instance, using the assumptions from Cussler (2009), the Stokes–Einstein equation yields a diffusion coefficient of $D_{O_2,H_2O} = 1.2 \times 10^{-9}\,m^2 \cdot s^{-1}$ for oxygen in water, whereas the Wilke–Chang correlation yields $D_{O_2,H_2O} = 2.2 \times 10^{-9}\,m^2 \cdot s^{-1}$ for the same system at $T = 20\,°C$. More importantly, Eq. 2 assumes a constant diffusion coefficient. However, this is not always reasonable, considering diffusion coefficients are concentration-dependent (Cussler 2009; Bardow et al. 2005; Bothe and Druet 2023). As time progresses and the concentration gradient diminishes, the diffusion coefficient is no longer measurable (Bardow et al. 2005). We consider small-scale phenomena that occur over a rather short period of time and are, hence, transient. Therefore, the concentration dependence of the diffusion coefficient should be kept in mind when discussing the results, whilst considering that this is however not the main focus of the current work.

In the current study, dissolved oxygen concentration fields around stationary oxygen bubbles in physically degassed water are measured applying PLIF in a light sheet fluorescence microscope. The oxygen bubbles have approximate diameters of $d_B \approx 220$ µm, highlighting the small scales on which the measurements are carried out. The study will exhibit how transport via sole diffusion can be visualised and analysed with a high spatial resolution on a micrometre scale. Furthermore, the applicability of LSFM for studies on multiphase transport phenomena will be proved. We emphasise that the focus of this publication is to introduce and validate a novel experimental application of LSFM by resolving dissolved oxygen concentrations in the vicinity of a single bubble on a local scale. Although some future analyses will be briefly mentioned and described, their details and quantification are, however, not within the scope of this work.

3 Methods

3.1 Light sheet fluorescence microscopy

The LSFM (*Rapp Optoelectronic GmbH*, Germany) consists of a laser with light sheet optics and a microscope for the imaging (Fig. 1). The applied laser is a continuous-wave diode laser (DL-488/100/OLX2, *Rapp Optoelectronic GmbH*, Germany) with a wavelength of $\lambda = 488$ nm. The laser beam is focussed to a light sheet with a minimal thickness of $\delta_L = 5$ µm in the focal point, depicted schematically along with its width and height in Fig. 1b. As discussed in Sect. 2.1, such a thin light sheet is a novelty within the field of multiphase process engineering and fluid dynamics and, therefore, enables new studies on a microscopic scale. The imaging system is flexible and can be adjusted to the individual experimental requirements. It is possible to use any high- or low-speed camera for the imaging, as well as any microscopy lens. In this way, the spatial and temporal resolutions can be chosen flexibly. The components of the imaging system used in the current study are listed in Table 1 along with other experimental specifications. Although the chosen camera (Imager CX2-5, *LaVision GmbH*, Germany) allows an imaging frequency of up to at least $f = 793$ Hz, a temporal resolution of $f = 5$ Hz is considered sufficient for the current study, as low dynamics are expected. To capture the bubble outline and its coordinates as clearly as possible, every second image is illuminated with a LED-panel from the back (see Fig. 2 in Sect. 3.2). Therefore, the overall imaging rate, as listed in Table 1, is $f = 10$ Hz, but images illuminated with the laser are available at a rate of $f = 5$ Hz. Respectively, this also applies for images illuminated with the LED-panel. The specific imaging system in this study achieves a pixel pitch of $s = 0.27\ \mu m \cdot px^{-1}$, measured using a calibration target

Table 1 Experimental specifications

Component	Specification
Camera	Imager CX2-5 (*LaVision GmbH*, Germany)
Lens	UPlanFL N 10x/0.3 (*Olympus Deutschland GmbH*, Germany)
Laser	Diode laser (DL-488/100/OLX2, *Rapp Optoelectronic GmbH*, Germany)
Laser wavelength	$\lambda = 488$ nm
Light sheet thickness	$\delta_L = 5$ µm
Maximal laser power	$P = 100$ mW
Synchronisation unit	PTU X (*LaVision GmbH*, Germany)
Imaging rate	$f = 10$ Hz
Exposure time	$t_e = 6$ ms
Laser and LED pulse time	$t_{LP/LED} = 3$ ms
Fluorescent dye	Dichlorotris(1,10-phenanthroline) ruthenium(II) hydrate (CAS: 207802-45-7, *Sigma Aldrich*, USA)
Concentration of dye	$\zeta_d = 30$ mg $\cdot$ L^{-1}, as in Kursula et al. (2022); Timmermann et al. (2016); Weiner et al. (2019)

(*Rapp Optoelectronic GmbH*, Germany) placed in the focal plane of the camera. In comparison, previous dynamic PLIF measurements on a microscopic scale achieved pixel pitches of $s = 12.9$ µm·px^{-1} (Dani et al. 2007) or $s = 2.3$ µm·px^{-1} (Francois et al. 2011). Evidently, new possibilities are opened up with respect to spatial resolution using LSFM. The current work shows how LSFM can resolve concentration boundary layers on a microscopic scale. More spatial resolutions of LIF measurements are listed by Rüttinger et al. (2018). Additionally, compared to applications in the field of biology (Olarte et al. 2018; Strobl and Stelzer 2014), the spatial resolution presented ranks rather high.

For measurements on a microscopic scale, a few particular considerations have to be made in order to ensure reliable and reproducible results. Firstly, the precise adjustment of the respective focal points of the laser and the camera onto the measurement plane of the sample is crucial. For this purpose, all laser and camera optics are mounted on 2D translation stages (Two-Axis Linear Translation Stage XYT1/M, *Thorlabs GmbH*, Germany), which allow a precise positioning of the focal points in space on a micrometre scale. Additionally, the laser optics allow a vertical positioning of the light sheet path. The sample is placed on a 3D translation stage (3-Axis Rollerblock Stage RB13P1/M, *Thorlabs GmbH*, Germany). The translation stages enable a precise alignment of the light sheet to the middle cross section of the bubble. On this two-dimensional plane, the diffusion of dissolved oxygen in the liquid can be observed in the radial direction from the bubble centre in space and time.

Secondly, any vibrations, appearing as large movements of the sample on a microscopic scale, coming from the environment of the set-up have to be minimised. The LSFM is, hence, placed on a damping optical breadboard (Nexus Breadboard, *Thorlabs GmbH*, Germany) mounted on air-filled passive isolation mounts (Standard-Duty Passive Isolation Mount, *Thorlabs GmbH*, Germany). This way, vibrations coming from the surroundings are damped and a stable field of view throughout the whole measurement time is ensured.

Lastly, whenever a dissolved fluorescent dye absorbs laser light, heat convection induced by the absorbed energy can pose a challenge. A buoyancy-driven flow of the liquid, caused by the decreasing density as a response to the increasing temperature, distorts any measured concentration field. To prevent heat convection, the time for which the sample is exposed to the laser power input should be minimised, whilst preserving a sufficient exposure time for the imaging. In the current study, this is achieved by pulsing the laser and, thus, shortening the time for which the liquid is exposed to the power of the laser. Therefore, the energy absorbed by the liquid phase is sufficiently low to prevent the occurrence of heat convection. The pulsing is realised by triggering the cw-laser with a 5 V TTL pulse signal synchronised to the imaging rate. Both, the triggering as well as the synchronisation, are controlled with the synchronisation unit PTU X (*LaVision GmbH*, Germany) and the software DaVis 11 (*LaVision GmbH*, Germany). The prevention of heat convection can easily be validated by observing the movement of flow-following fluorescent microparticles in the liquid, as in various flow measurement techniques such as PIV or PTV. Such a validation is provided in the Supplementary Information S1 (Kursula et al. 2026b).

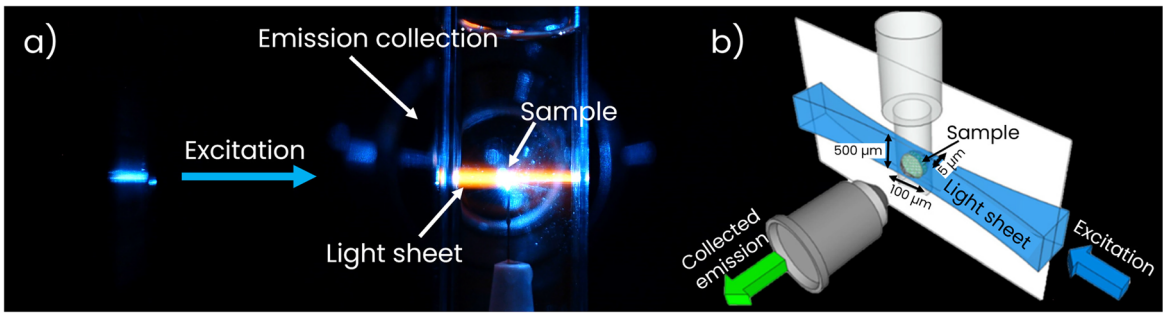

Fig. 1 **a** Excitation and collection of the emission of a sample with the LSFM used in the current study, **b** Scheme of the light sheet dimensions, adapted from (Olarte et al. 2018)

Although LSFM is widely applied for studies of biological systems, the impact of convection, or generally heating effects, on the measurements has, interestingly, not yet been discussed in literature to our knowledge. Solely the prevention of phototoxicity of the laser beam on the samples is frequently mentioned. To avoid any damage of the biological samples, Stelzer has proposed a limit of 100 $\mathrm{mW \cdot cm^{-2}}$, corresponding to the solar constant to which life on earth has adjusted (Stelzer 2015). However, in the current study we do not use any biological samples where possible damages need to be considered. As detailed above, just the absorption of the laser energy by the liquid has to be sufficiently low to not induce heat convection.

Revising the specifications of the components used for LSFM here, two major limitations might appear for some applications, although not in the current one. Obviously, the spatial resolution can pose a limitation, if high gradients cannot be resolved sufficiently. A lens with a higher spatial resolution also needs a higher light intensity. A need for high light intensity can pose a major limitation when applying LSFM for process engineering problems. As detailed above, the absorption of laser light can lead to heat convection, but also to photobleaching as well as phototoxicity, if biological samples are used. With the specifications chosen for the current study, these limitations are overcome, as discussed in this Sect. 3.3.

3.2 Experimental set-up and procedure

The experimental set-up used in the current study is depicted in Fig. 2. Since the LSFM is already detailed in Sect. 3.1, this section focuses on the remaining parts of the set-up.

A significant consideration is the selection of the measurement cell in which the sample is positioned. For the camera and the laser sheet being aligned at a 90° angle, as depicted in Fig. 1, two optical paths are required. The mass transfer from a single oxygen bubble is, thus, studied in a standard spectroscopy cuvette (UV grade PMMA cuvette, *Kartell Spa*, Italy). The cuvette has four transparent windows for the required two optical paths for excitation and emission collection (see Fig. 1).

The oxygen bubble is generated using a fused silica capillary (Fused Silica Capillary, *Postnova Analytics GmbH*, Germany) with an inner diameter of $d_{\mathrm{I,c}} = 2$ µm and pressurised oxygen. Prior to the bubble generation, the PTFE tubing (No-Ox tubing GasTight, *Techlab GmbH*, Germany) is flushed with oxygen to remove the air and ensure the generation of a pure-oxygen bubble. The pressurised oxygen flow is controlled with a mass flow controller (EL-FLOW Select F-201CV, *Bronkhorst High-Tech B.V.*, Netherlands). To stop the growth of the bubble, it is not sufficient to stop the oxygen flow, but the pressure from the tubing has to be released. For this, a three-way valve is used (V1 in Fig. 2).

To establish the highest possible driving force for the mass transfer between the oxygen bubble and the water and to avoid cross-diffusion, the water is physically degassed prior to the experiment. First, the oxygen-sensitive fluorescent dye (Table 1) is dissolved in water. Subsequently, the water-dye solution is degassed in the measurement cell by drawing a vacuum with a vacuum pump for ten minutes. This way, after breaking the vacuum, a dissolved oxygen concentration of $c_{\mathrm{O_2}} < 1.5$ ppm is ensured, measured with an in-house built oxygen probe (oxygen sensor: SP-PSt3-NAU-D5-OIW, *PreSens Precision Sensing GmbH*, Germany). Diffusion of oxygen or other gases from the ambient air into the liquid phase is considered negligible, because the measurement is started immediately after breaking the vacuum. Vacuum treatment of water can cause evaporation-induced convection (Song and Nobes 2011), which can influence mass transfer measurements on this small scale. However, such effects are not expected in the current work,

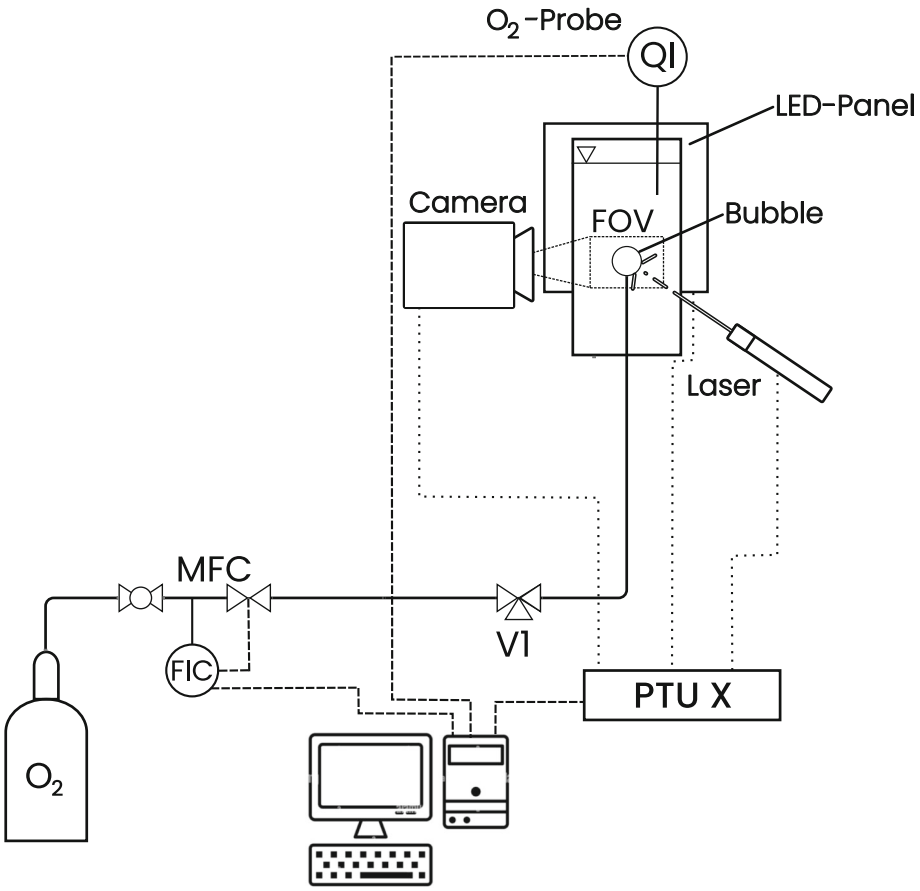

Fig. 2 Experimental set-up

because the vacuum is broken after the water is degassed and the measurement is conducted at ambient pressure.

For the calibration of the captured fluorescence intensities to known dissolved oxygen concentrations in the liquid phase, defined dissolved oxygen concentrations are needed. This is realised by carefully mixing defined ratios, presented in Table 2, of degassed and oxygen-saturated water. Subsequently, the fluorescence intensity of the mixture is captured in the measurement cell. This calibration is performed for five concentrations of dissolved oxygen, listed in Table 2. The concentrations are calculated from the respective ratios of oxygen-saturated and degassed water.

3.3 Planar laser-induced fluorescence

In planar laser-induced fluorescence measurements, a fluorescent tracer is excited and its emission is captured with a camera. For measurements of dissolved oxygen concentration fields, an oxygen-sensitive fluorescent dye is dissolved into the liquid. When in contact with oxygen, the fluorescence of the dye is quenched, resulting in darker areas in the captured images, as visible in Fig. 3a. This allows the observation of the evolution of dissolved oxygen concentrations in the liquid phase in space and time. The dye chosen in the current study is a ruthenium complex (see Table 1), which has its maximal light absorption at a wavelength of $\lambda_{abs} = 449$ nm and maximal emission at a wavelength of $\lambda_{em} = 582$ nm (Rüttinger et al. 2018), at which the camera used has an approximate quantum efficiency of $QE \approx 65\%$. An analysis of the photobleaching during the measurements is provided in the Supplementary Information S1. Detailed reviews of available fluorescent dyes can be found in (Rüttinger et al. 2018) and (Xu et al. 2020). To ensure that the camera captures the sole red fluorescence emitted by the liquid, and no blue reflections, a 500 nm long-pass filter is used. The remaining reflections in the system cannot be prevented; however, they can be identified easily, as indicated in Fig. 3b.

Table 2 Mixing ratios of oxygen-saturated and degassed water and the resulting dissolved oxygen concentrations at $T = 20\,°C$ used for the calibration

Number	Volumetric mixing ratio of oxygen-saturated and degassed water / –	Calculated dissolved oxygen concentration c_{O_2} / mg · L^{-1}
1	0:1	0.0
2	1:10	4.16
3	1:1	22.9
4	3:1	34.35
5	1:0	45.8

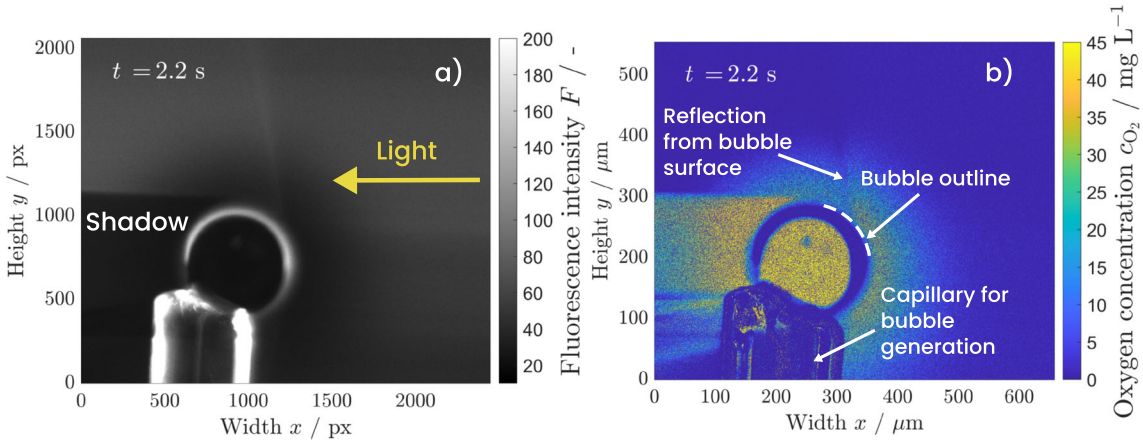

Fig. 3 **a** Raw image captured with the LSFM. The fluorescence quenching can be observed on the right-hand side of the bubble, indicating a high dissolved oxygen concentration in the liquid phase, **b** exemplary image after the pixel-wise calibration of fluorescence intensity to the local concentration of dissolved oxygen

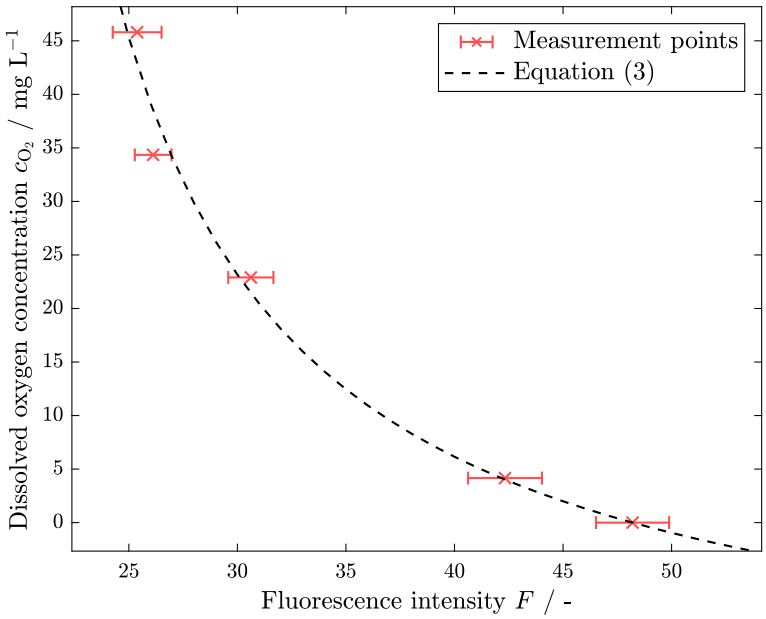

Fig. 4 Exemplary calibration curve for the dissolved oxygen concentration over the captured fluorescence intensity for the pixel with the coordinates $x = 1600$ px and $y = 600$ px in Fig. 3a

LIF measurements enable a fairly easy calibration of a specific fluorescence intensity to a defined dissolved oxygen concentration. For this calibration, a defined amount of oxygen is dissolved in the liquid phase and the fluorescence intensity is captured, as detailed in Sect. 3.2. Therefore, for each pixel, the

captured fluorescence intensity can be assigned to a local dissolved oxygen concentration, as in (Kursula et al. 2022; Kapoustina et al. 2019). First, to reduce noise, for each of the five calibration concentrations an average of 100 images is generated. Next, calibration curves for each individual pixel i are computed by fitting the measurement points.

The equation chosen for the calibration curve is

$$c_{O_2,i}(F) = \left(f_{a,i} K_{a,i} \left(\frac{F_{0,i}}{F_{0,i} - F} - \frac{1}{f_{a,i}} \right) \right)^{-1}, \tag{3}$$

where $c_{O_2,i}$ is the dissolved oxygen concentration in the liquid phase, $F_{0,i}$ the fluorescence intensity of pixel i in absence of the quencher, F the fluorescence intensity at the dissolved oxygen concentration and $f_{a,i}$ and $K_{a,i}$ are fitting parameters. Equation 3 is a modified version of the well-known Stern–Volmer equation (Stern and Volmer 1919), as presented in (Lakowicz 2010). The modification is applicable whenever a fraction f_a of the fluorescence is not accessible to the quencher, giving a new Stern–Volmer constant K_a. In such cases, the Stern–Volmer plot shows a downwards curvature for high concentrations of the quencher (Lakowicz 2010). In the current study, this behaviour of the Stern–Volmer plot is identified, as also visible in (Lakowicz 2010) for the fluorescent dye used. Therefore, Eq. 3 is used for the calibration curves instead of the standard Stern–Volmer equation.

The measurements are calibrated by applying the calibration curve of each pixel for each time step. Additionally, a Gaussian image smoothing in space is applied after the calibration to reduce the noise. For this, a standard deviation of $\sigma = 0.75$ of the Gaussian distribution is chosen for a smoothing over 5 pixels, corresponding to approximately 1.5 micrometres. The codes including the processing of the data are published in GitLab (see Code availability).

Figure 3b shows a calibrated, non-smoothed dissolved oxygen concentration field around the bubble. It is important to note that the relevant area for analysing the dissolved oxygen concentration fields is located on the right-hand side of the bubble, as this is the area with minimal reflections and shadowing.

4 Results

4.1 Concentration field around an oxygen bubble

The oxygen bubbles generated in the three measurements have initial diameters of $d_B = 223 \pm 4$ µm (SD), meaning a high reproducibility of the bubble sizes. Figure 5 shows the two-dimensional evolution of the dissolved oxygen concentration field around an oxygen bubble in degassed water over time measured with the LSFM. Firstly, it is important to highlight the small scales that can be observed with a high spatial resolution in these images. The oxygen bubble and the diffusion of the dissolved oxygen into the liquid bulk can be observed in time with a pixel pitch of $s = 0.27$ µm·px^{-1}. Such high-resolution measurements, with an option for also higher temporal resolutions, are unique within the field of multiphase mass transfer and fluid dynamics, as also highlighted in Sect. 3.1.

Furthermore, it is worth emphasising that no heat convection induced by the absorbed laser energy can be observed. The dissolved oxygen concentration front is evolving spherically and isotropically around the bubble. In case of occurring heat convection, the liquid would be flowing upwards, as detailed in Sect. 3.3. Since the dissolved oxygen acts as a nearly perfect flow-following tracer, the concentration field would evolve rather vertically, not spherically, in case of heat convection. Considering the small scales studied here, where each minimal movement can be seen, this achievement deserves particular attention and should not be undervalued.

One effect that might have an impact on the mass transfer of oxygen is the gradient in surface tension near the contact point of the bubble with the capillary. Although no Marangoni convection is observed here, the mass transfer of dissolved oxygen at the contact point could still be enhanced. However, such effects are neglected here. Marangoni convection induced by the gradient in surface tension can be ruled out, because the dissolved oxygen, a near-perfect flow tracer, does not exhibit any circulating structures near the bubble, as shown in Fig. 5.

The data presented in Fig. 5 facilitate a detailed quantitative spatio-temporal analysis of the dissolved oxygen concentrations in the liquid phase. This can be done by observing the temporal evolution of the dissolved oxygen concentrations in the liquid phase along the radius of the bubble. Figure 6a shows the concentrations of dissolved oxygen in the liquid phase along the r-coordinate at the height of the bubble

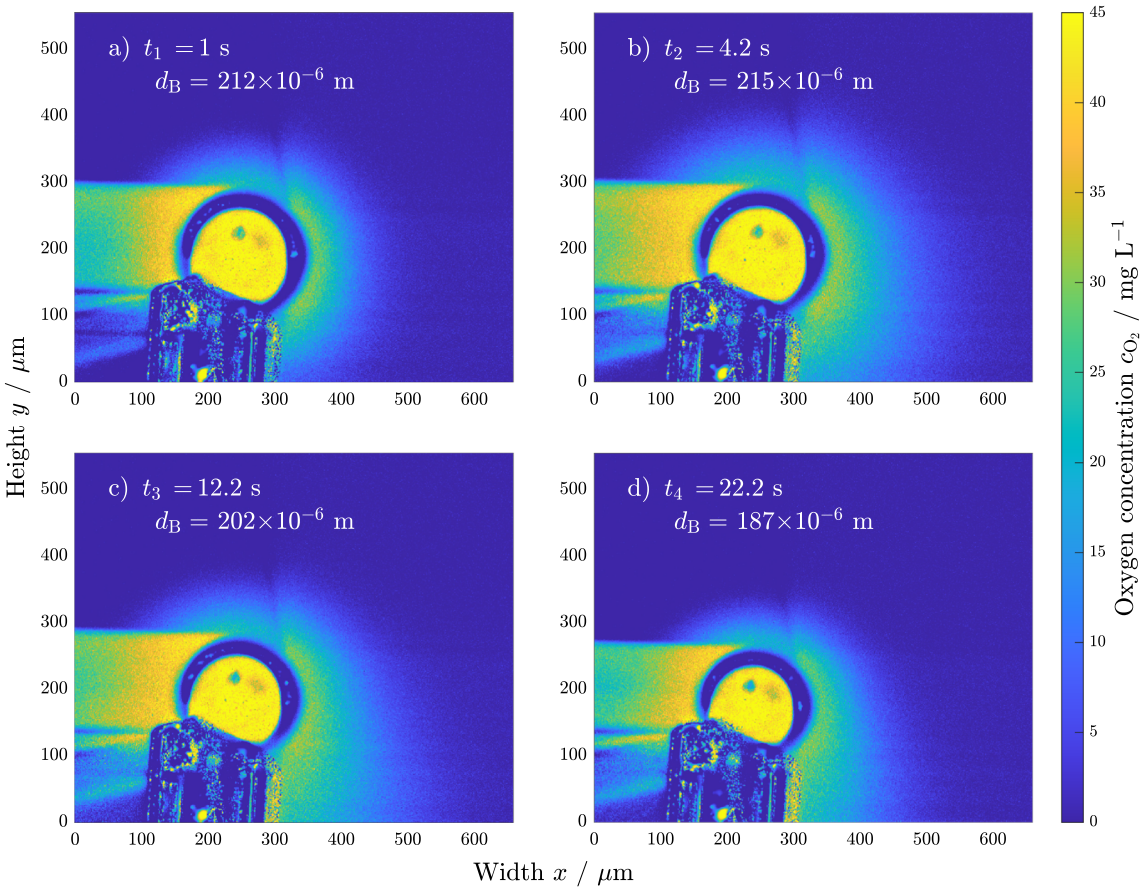

Fig. 5 Concentration field of dissolved oxygen around an oxygen bubble in dissolved water for time points **a** t_1 = 1 s, **b** t_2 = 4.2 s, **c** t_3 = 12.2 s and **d** t_4 = 22.2 s

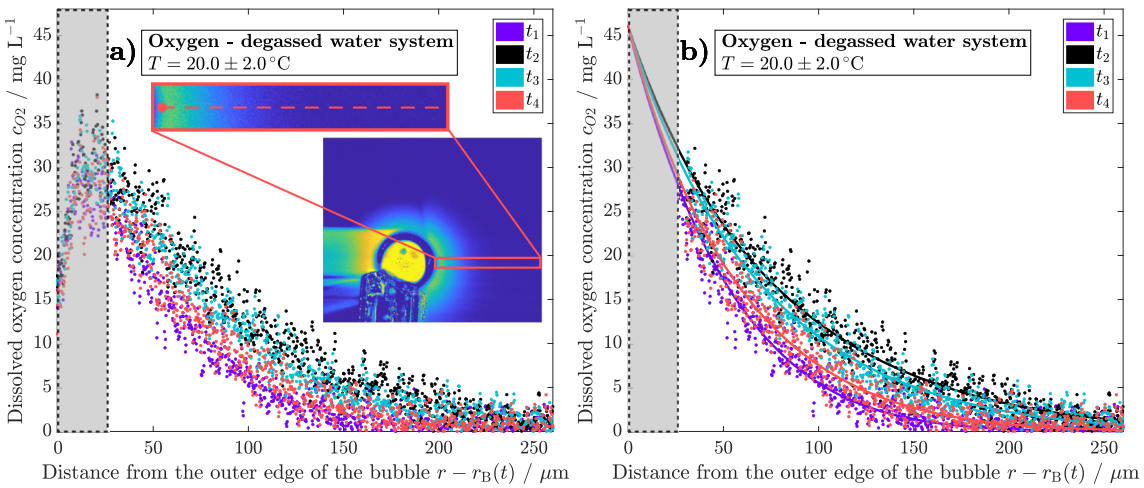

Fig. 6 Concentration of dissolved oxygen in the liquid along the line depicted in **a** for time points t_1 = 1 s, t_2 = 4.2 s, t_3 = 12.2 s and t_4 = 22.2 s. Grey area marks the area of high uncertainty due to reflections from the bubble surface. **a** Unfiltered data in the vicinity of the bubble, **b** filtered data and fitting of concentration curve with forcing through the saturation concentration $c^*_{O_2}$ = 45.8 mg · L^{-1} at $r = r_B$

centre, starting from the gas–liquid interface $r = r_B$, as depicted in the subfigure. It is noticeable that the concentrations in the vicinity of the bubble seem to be dropping. Physically, the concentration at the

interface $r = r_B$ should equal the saturation concentration of oxygen in water $c^*_{O_2} = 45.8\ \mathrm{mg \cdot L^{-1}}$ at the approximate ambient temperature of $T = 20.0\ °C$. It is conceivable that some light reflections from the gas–liquid interface result in a higher local fluorescence intensity around the bubble and, thus after calibration, in a seemingly lower dissolved oxygen concentration. For this reason, in Fig. 6b the concentrations near the gas–liquid interface are filtered and Eq. 2 is fitted using the remaining points and forcing the curve through the saturation concentration at the interface. Here, the diffusion coefficient D_{O_2,H_2O} is used as fitting parameter and the time-dependent radius of the bubble $r_B = r_B(t)$ is taken from the experiments. The fitting here can be justified with the clear upwards trend of the concentration until the point of filtering and with the rather short distance between the last measured concentration value and the saturation concentration along the r-coordinate.

The described effect represents one limitation of LSFM for multiphase applications. For convective studies where the thickness of the concentration boundary layer is of interest, the range of bubble Reynolds numbers that can be studied is crucial. As in the current study, the range starts at Re = 0. However, it is difficult to provide an upper limit of bubble Reynolds numbers that can be studied. The Reynolds numbers are dependent on the bubble size and the velocity, which can both vary in the measurements. The described supposed reflections at the bubble interface may demonstrate a challenge for cases where the concentration boundary layer thickness falls below $\delta_c = 50\ \mu m$. Therefore, rather than considering a fixed Reynolds number as an upper limit, the thickness of the boundary layer should be large enough to provide a reliable foundation for a fitting of the concentration data, as in Fig. 6.

The concentration fields depicted in Fig. 5 and the curves in Fig. 6 show a fast spatial and temporal evolution of the dissolved oxygen concentration until the time point $t_2 = 4.2$ s. However, there does not seem to be a significant difference between the two time points t_2 and t_3, suggesting a somewhat steady state. It should be considered that the mass transfer from the bubble will eventually complete and, if reached at all, the steady state will not last long. After that, as the dissolved oxygen is diffusing into the liquid bulk, the concentration curves will evolve back towards zero again, indicated by the curves for time points t_3 and t_4.

To validate the measurements, and thus demonstrate the applicability of LSFM, the measured concentration curves are compared to the well-known diffusive transfer of oxygen to water described by Fick's law, as described in Sect. 2.2. For this, Eq. 2 is applied for the given points in time. Figure 7 shows a comparison between the measured and calculated concentration curves of dissolved oxygen. Contrary to Fig. 6, the experimental curves in Fig. 7 are mean values of three measurements. At first glance, the fit between the measured and calculated, theoretical concentration curves in Fig. 7 does not appear to be very satisfying for long times. However, there are some contributing factors that need to be accounted for when comparing the curves. Firstly, Eq. 2 is sensitive towards the experimentally obtained radius of the bubble $r_B(t)$, the chosen starting time point t_0 and the diffusion coefficient D_{O_2,H_2O}. These three uncertainties are considered in a Gaussian propagation of error, resulting in the depicted standard deviation of the calculated curves (red). The uncertainty in determining the radius of the bubble is estimated to be $\Delta r_B = 10$ px. Determining the correct starting point in time t_0 of the mass transfer from the images can be challenging, since the growth of the bubble is captured with an imaging frequency of $f = 5$ Hz. This leads to a uncertainty of t_0 of at least $\Delta t_0 = 0.2$ s, corresponding to the time between two images. The starting time point t_0 determines the curves that are compared in Fig. 7 and, especially for short times, the progression of the calculated concentration front from Eq. 2. The choice of the diffusion coefficient D_{O_2,H_2O} has an even greater impact on the curve progression, as briefly mentioned in Sect. 2.2. According to Xing et al. (2014), the mean experimental value of the diffusion coefficient of dissolved oxygen in water is $D_{O_2,H_2O} = 2.0 \times 10^{-9}\ \mathrm{m^2 \cdot s^{-1}}$ (2014), which is therefore the chosen value for the calculation using Eq. 2. Nevertheless, the diffusion coefficient can vary, especially due to the fluorescent dye dissolved in the liquid. In accordance with Cussler, the uncertainty of the diffusion coefficient is estimated to be 20% (Cussler 2009), meaning $\Delta D_{O_2,H_2O} = 0.4 \times 10^{-9}\ \mathrm{m^2 \cdot s^{-1}}$. Furthermore, considering the transient nature of the measurements presented in the current study, it would be more accurate to use time- or concentration-dependent diffusion coefficients in Eq. 2, as essentially done for the measurements by using the diffusion coefficient as fitting parameter. Secondly and more importantly, the lower detection limit (LOD) of LSFM must be considered, especially at faraway radial positions with low dissolved oxygen concentrations. Before discussing this in detail, the impact of the detection limit on the curves in Fig. 7 is described. In the current experiment, the source of oxygen is finite, and the surface area available for the mass transfer decreases with time. With negligible Laplace pressure for the bubble sizes in question, the mass transfer rate across the interface into the liquid stays constant, and therefore, the overall mass flow rate of oxygen decreases. Simultaneously, the dissolved oxygen in the liquid is diluted in the quasi-infinite volume of the liquid bulk. This leads to infinitesimally small dissolved oxygen

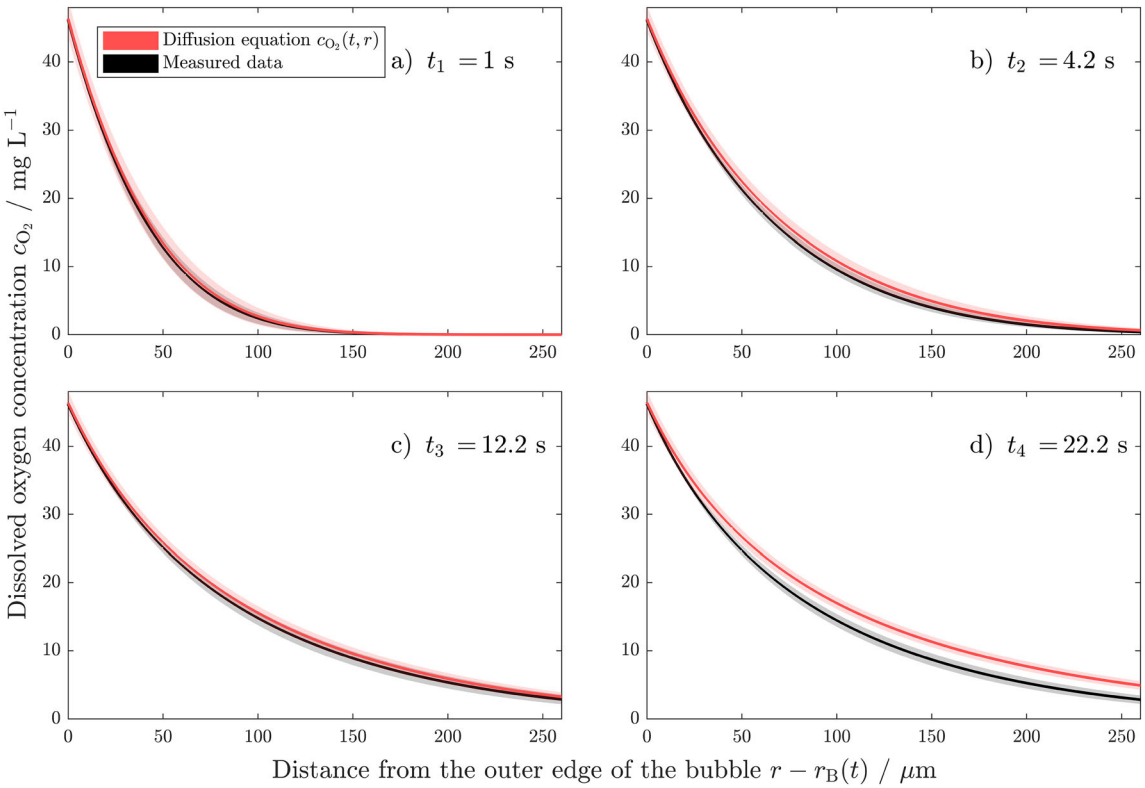

Fig. 7 Comparison between measured (black) and calculated (red) dissolved oxygen concentration over the radius, starting at the gas–liquid interface, at the time points **a** $t_1 = 1$ s, **b** $t_2 = 4.2$ s, **c** $t_3 = 12.2$ s and **d** $t_4 = 22.2$ s. The standard deviations of the measured data (grey) result from three measurements and the standard deviations of the calculated data (light red) are determined via a Gaussian error propagation

concentrations, which cause only a slight quenching of the fluorescence intensity and cannot be detected with LSFM. In conclusion, as these infinitesimally small concentrations of dissolved oxygen cannot be captured and the overall mass flow rate of oxygen from the bubble decreases with progressing time, the measured concentration curves eventually approach zero again. This explains the increasing deviations between the curves for increasing times in Fig. 7.

As discussed above, the deviations between the measured and calculated concentrations in Figs. 7 and 8 may emerge from the reduced detection of low dissolved oxygen concentrations. Therefore, a short consideration of the image quality in terms of signal-to-noise ratio (SNR) and intensity fluctuations is necessary. As described in Sect. 3.3, the camera used has a fairly high quantum efficiency at the emission wavelength of the dye and the noise is specified as two electrons per pixel. However, as visible in Fig. 4, the fluorescence intensities captured are rather low. This is a consequence of the short exposure times necessary to avoid heat convection, as discussed in Sect. 3.1. Therefore, for the SNR, low values of SNR < 10 are expected. For low dissolved oxygen concentrations, the fluctuations in fluorescence intensity are rather high, as indicated by the error bars in Fig. 4, but also visible in Fig. 6. However, as described in Sect. 3.3, for the calibration, averaged images of $n_{\mathrm{img}} = 100$ are created. The SNR is known to increase by a factor of $\sqrt{n_{\mathrm{img}}}$, meaning that, at least in the calibration, the SNR is acceptable. In the evaluation of the images, the noise is reduced by a Gaussian image smoothing over 5 pixels, over which no significant change of the fluorescence intensity, and respectively dissolved oxygen concentration, is expected. Furthermore, for the presented analysis, Eq. 2 is fitted to the experimental data, which means that the fluctuations of the data that emerge from the noise are further smoothed and lose impact. After these measures, the resulting effective SNR is considered sufficient and the data accurate enough for the fitting conducted. Looking again at the intensity fluctuations in Fig. 4, the uncertainty in the measured dissolved oxygen concentration can be approximated by $\Delta c_{O_2} \approx 2\,\mathrm{mg} \cdot \mathrm{L}^{-1}$. A common criterion for the LOD is determining the concentration at which the fluorescence quenching equals three times the standard deviation of the fluorescence intensity at $F = F_0$.

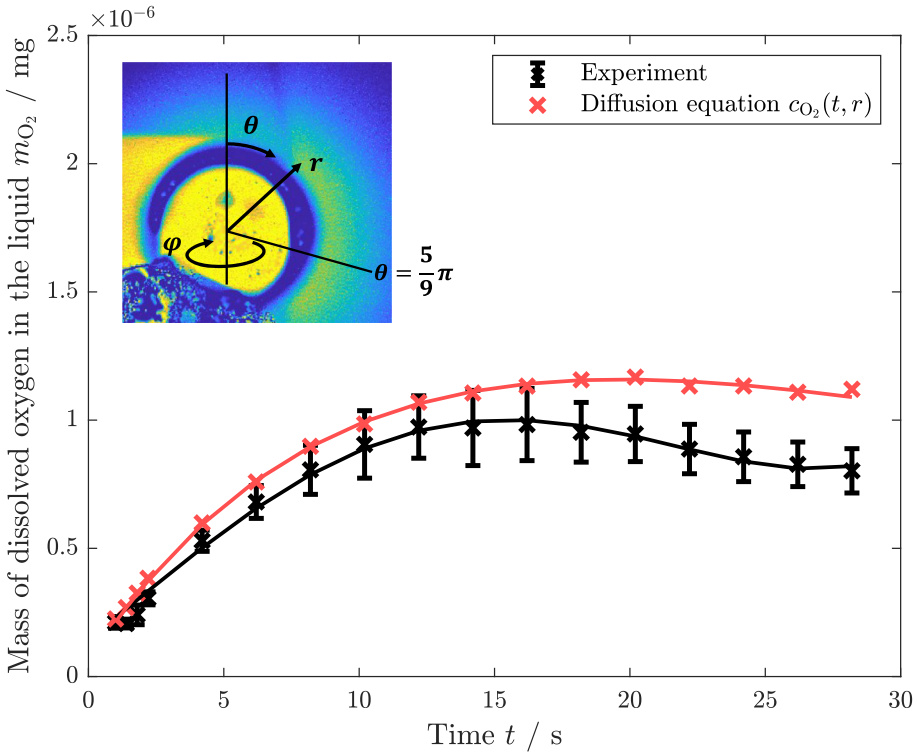

Fig. 8 Measured (black) and calculated (red) instantaneous total mass of oxygen transferred in the liquid phase over time. The mass of oxygen is integrated for each point in time over the depicted sphere's coordinates r, φ and θ. The standard deviation of the measured data results from three measurements

Here, the standard deviation at $F = F_0$ is SD = 1.68. Therefore, the lowest detectable quenching is $\Delta F = 5$ and the respective LOD concentration at a quenching $F_{\mathrm{LOD}} = F_0 - \Delta F$ is approximately $c_{O_2}(F_{\mathrm{LOD}}) = 3.5\,\mathrm{mg} \cdot \mathrm{L}^{-1}$. For reliable measurements, it is necessary to obtain enough high dissolved oxygen concentrations for an accurate fitting of the concentration curve that can balance out the possibly erroneous, low concentrations.

To validate the measurements within the boundaries of the detection limit, the total mass of dissolved oxygen transferred to the liquid volume is calculated. This is done by an integration of the concentration curve over the spherical volume

$$m_{O_2} = \int_0^{\frac{5}{9}\pi} \int_0^{2\pi} \int_{r_B}^{r_2} c_{O_2}(t_i, r) r^2 \sin(\theta)\, \mathrm{d}r\, \mathrm{d}\varphi\, \mathrm{d}\theta, \tag{4}$$

where r, φ and θ are the spherical coordinates, according to the subfigure of Fig. 8, and t_i is the chosen point in time. Along the radial coordinate r, the integration is conducted from the interface to $r_2 = r(c_{O_2} < \mathrm{LOD}, t)$, corresponding to the point in space where the concentration of dissolved oxygen falls below the LOD for each point in time. To account for the volume below the bubble where the oxygen neither can transfer nor can its concentration be measured due to the capillary, Eq. 4 is integrated from 0 to $\frac{5}{9}\pi$ along the θ-coordinate, as depicted in the subfigure of Fig. 8. Figure 8 shows the instantaneous mass of dissolved oxygen in the liquid volume over time for both the theoretical approach and the measured values. For short times, both curves show the transient beginning of the mass transfer. After that, the mass of dissolved oxygen in the field of view calculated using Eq. 2 levels off. The experimental curve levels off and, with increasing time, the mass of dissolved oxygen even starts to decrease. The flattening of the curve can be explained by a decreasing mass flow rate of oxygen from the bubble. It is good to revise the infinite dilution of the dissolved oxygen into the liquid bulk. As the dissolved oxygen is diluted and the concentration falls below the LOD, the concentration of dissolved oxygen is not detected and seems to be lost. Whilst the mass flow rate of oxygen from the bubble decreases over time, more dissolved oxygen apparently exits the mass balance by dilution than enters from the bubble. This causes an overall decrease in the total

mass of dissolved oxygen detected. Therefore, it is questionable whether the data for times larger than $t = 15$ s can be used for the validation and a sufficient fit within the boundaries of the detection limit can be concluded. Also, especially because the measured and calculated dissolved oxygen concentrations at short times match well, a possible deviation emerging from the constant diffusion coefficient used for the theoretical approach should not be neglected. With a concentration-dependent diffusion coefficient, the curve calculated with the theoretical approach could also exhibit a downwards trend for increasing time. It is conceivable that the deviations result from a combination of the detection limit in the experiments and the constant diffusion coefficient in the calculation.

Considering the points presented above, the curves in Figs. 7 and 8 show a sufficient match between the theory and measured values within the detection limits of LSFM. For long times and low dissolved oxygen concentrations, the measurement system reaches its limits in this case. LSFM is therefore considered applicable in mass transfer studies where enough high dissolved oxygen concentrations can be obtained to balance the concentrations below the detection limit. All in all, the exemplary measurement and the comparison to a well-known diffusion-only case are considered suitable to demonstrate the applicability of LSFM for mass transfer studies on a microscopic scale.

4.2 Further research possibilities in multiphase systems

The measurements introduced in this work open up many new possibilities for further studies and analyses. The current publication focuses on the applicability of LSFM and the validation of the corresponding data using a well-known case, not on the interpretation with respect to process engineering applications. Therefore, in the following, a few approaches for such interpretations will be briefly presented to highlight the new possibilities that we consider meaningful.

As already discussed above, Fig. 8 shows the amount of dissolved oxygen transferred into the liquid over time. Whilst the comparison with the theoretical amount of oxygen transferred can be used for the validation of the accuracy of the measurements, such curves can also quantify the impact the bubble size has on the mass transfer performance over time. For a theoretical thought experiment underlining this effect, two considerations are introduced. Firstly, compared to a single small bubble, a single larger bubble will transfer more oxygen into the liquid over time, and the mass transfer process will last for a longer time period. This is simply explained by the larger gas volume in the bubble and a larger interfacial surface area between the gas and liquid when comparing single bubbles. Secondly, the time in Fig. 8 can be considered as the residence time of the bubble in an aerated bioreactor. It immediately becomes evident that the smaller bubble will complete its mass transfer early in its residence time. The distance covered by the small bubble in a bioreactor during this fraction of the residence time is fairly short. Small bubbles for aeration can, therefore, lead to an inhomogeneous distribution of dissolved oxygen in a bioreactor. In contrast, the mass transfer from the larger bubble is distributed more homogeneously over its residence time and, analogously to the reasoning above, also in the reactor. For an industrial-sized bioreactor, this means that, although the efficiency of mass transfer increases with a larger volume-specific interfacial area, the effectiveness of very small bubbles for aeration is not necessarily given. It is questionable whether this can be quantified with global methods, like, for instance, the volumetric mass transfer coefficient, as they usually do not account for local inhomogeneities. The methods introduced in the current publication enable detailed studies of the described phenomenon, including convective mass transfer. Specifically, the data enable an analysis of time- and angle-resolved concentration gradients at the gas–liquid interface and, therefore, time- and angle-resolved local Sherwood numbers, as presented by Brauer and Mewes (1971), as well as resolving concentration boundary layers in convective systems. This way, the combined convective and diffusive mass transfer performance of bubbles, for instance with varying sizes, over time can be quantified. In convective systems, the already discussed limitation of the boundary layer thickness due to reflections from the interface needs to be accounted for.

Furthermore, LSFM can be used for studies on fluid dynamics in microscopic multiphase systems. Exemplarily, Marangoni convection can influence the mass transfer performance in gas–liquid systems where gradients in the surface tension exist. Studies that previously needed numerical support, as conducted by Baczyzmalski et al. (2017), can now be complemented by experimental concentration and flow data on the microscopic scale.

Within this publication, we present high-resolution spatio-temporal data of oxygen mass transfer on a microscopic scale. Such data can be used to study diffusion in a range of systems. On the one hand, the briefly discussed sensitivity and spatio-temporal change of the Fick's diffusion coefficient can be studied

locally. On the other hand, the impact of dissolved process gases in the liquid bulk, as found in aerated bioreactors, on the desired mass transfer performance can be studied on a local scale. As these gaseous species are also striving for a thermodynamic equilibrium, they are diffusing into the gaseous phase, supposedly influencing the desired mass transfer performance (Matthes 2021; Karnbach et al. 2016). Using LSFM, these effects can be quantified on a local and microscopic scale by capturing the local dissolved oxygen concentrations in the liquid phase, as exhibited in the current work. The effects can also be quantified by determining the Fick's diffusion coefficients of the dissolved oxygen for these systems. The diffusion coefficients vary depending on the species in the system, as will be presented in a follow-up paper.

Finally, such data as presented in the current study are suitable benchmark data for the validation of numerical simulations. As computational methods have an increasing importance in today's research, their validation must be considered as well. For this purpose, high-resolution data, as presented here, are necessary.

5 Conclusion

Within the scope of this publication, we introduced the first experimental application of LSFM for studies of microscopic gas–liquid transport phenomena. LSFM enables PLIF and PIV measurements on a microscopic scale with a submicron pixel pitch, from which concentration boundary layers and flow dynamics in the vicinity of interfaces can be resolved.

In an exemplary study, the diffusive transport of dissolved oxygen from a single bubble into the liquid bulk was resolved on a micrometre scale. The study proves the applicability of LSFM for studies of multiphase transport phenomena and highlights the advantages compared to other state-of-the-art technologies within the field. Limitations of LSFM for the aimed purposes are discussed. It is evident that LSFM, and the high-resolution data obtained with it, opens up a range of new possibilities for transport studies on a microscopic scale, of which we describe just a few. We expect to deepen our fundamental understanding of the governing transport phenomena on a microscopic scale by using LSFM in the future.

Supplementary Information The online version contains supplementary material available at https://doi.org/10.1007/s12650-026-01115-7.

Acknowledgements Funded by the Deutsche Forschungsgemeinschaft (DFG, German Research Foundation)—project 501131738. We thank student assistant Sayaka Takagi for her excellent work and efforts in the laboratory.

Author contributions Lotta Kursula was involved in data curation, formal analysis, investigation, methodology, software, validation, visualisation, and writing—original draft preparation. Felix Kexel took part in investigation, methodology, supervision, and writing—review and editing. Marko Hoffmann participated in conceptualisation, funding acquisition, project administration, and writing—review and editing. Niklas-Maximilian Epping was involved in writing—review and editing. Paul Bubenheim was responsible for funding acquisition and writing—review and editing. Koichi Terasaka contributed to conceptualisation and writing—review and editing. Andreas Liese participated in conceptualisation, funding acquisition, project administration, and writing—review and editing. Michael Schlüter took part in conceptualisation, funding acquisition, project administration, resources, supervision, and writing—review and editing.

Funding Open Access funding enabled and organized by Projekt DEAL. Deutsche Forschungsgemeinschaft (DFG, German Research Foundation)

Data availability Data are published under the DOI https://doi.org/10.15480/882.15833 (Kursula et al. 2026a) and are available at TUHH Open Research (TORE) https://tore.tuhh.de/home.

Code availability Codes are available at https://collaborating.tuhh.de/v5/reactive-bubbly-flows/lotta-kursula/codes-for-lsfm-evaluation/.

Declarations

Conflict of interest The authors declare no conflict of interest.

Consent to participate Not applicable.

Consent for publication All authors have read the manuscript and have agreed to its publication.

Ethical approval Not applicable.

References

Alberini F, Liu L, Stitt EH et al (2017) Comparison between 3-D-PTV and 2-D-PIV for determination of hydrodynamics of complex fluids in a stirred vessel. Chem Eng Sci 171:189–203. https://doi.org/10.1016/j.ces.2017.05.034

Albert-Smet I, Marcos-Vidal A, Vaquero JJ et al (2019) Applications of light-sheet microscopy in microdevices. Front Neuroanat. https://doi.org/10.3389/fnana.2019.00001

Alméras E, Cazin S, Roig V et al (2016) Time-resolved measurement of concentration fluctuations in a confined bubbly flow by LIF. Int J Multiph Flow 83:153–161. https://doi.org/10.1016/j.ijmultiphaseflow.2016.03.011

Baczyzmalski D, Karnbach F, Mutschke G et al (2017) Growth and detachment of single hydrogen bubbles in a magnetohydrodynamic shear flow. Phys Rev Fluids 2(9):093701. https://doi.org/10.1103/PhysRevFluids.2.093701

Bardow A, Göke V, Koß HJ et al (2005) Concentration-dependent diffusion coefficients from a single experiment using model-based Raman spectroscopy. Fluid Phase Equilib 228–229:357–366. https://doi.org/10.1016/j.fluid.2004.08.017

Berrocal E, Kristensson E, Zigan L (2018) Light sheet fluorescence microscopic imaging for high-resolution visualization of spray dynamics. Int J Spray Combust Dyn 10(1):86–98. https://doi.org/10.1177/1756827717734078

Blutke A, Sun N, Xu Z et al (2020) Light sheet fluorescence microscopy guided MALDI-imaging mass spectrometry of cleared tissue samples. Sci Rep 10(1):14461. https://doi.org/10.1038/s41598-020-71465-1

Bothe D, Druet PE (2023) On the structure of continuum thermodynamical diffusion fluxes-A novel closure scheme and its relation to the Maxwell-Stefan and the Fick-Onsager approach. Int J Eng Sci 184:103818. https://doi.org/10.1016/j.ijengsci.2023.103818

Brauer H, Mewes D (1971) Stoffaustausch einschliesslich chemischer Reaktionen. Sauerländer, google-Books-ID: E0_WoAEACAAJ

Busciglio A, Grisafi F, Scargiali F et al (2010) On the measurement of bubble size distribution in gas-liquid contactors via light sheet and image analysis. Chem Eng Sci 65(8):2558–2568. https://doi.org/10.1016/j.ces.2009.12.031

Cussler EL (2009) Diffusion: mass transfer in fluid systems. Cambridge University Press, Cambridge

Dai H, Yang X, Schwarzenberger K et al (2025) Wettability-dependent dissolution dynamics of oxygen bubbles on Ti64 substrates. Int J Heat Mass Transf 236:126240. https://doi.org/10.1016/j.ijheatmasstransfer.2024.126240

Dani A, Guiraud P, Cockx A (2007) Local measurement of oxygen transfer around a single bubble by planar laser-induced fluorescence. Chem Eng Sci 62(24):7245–7252. https://doi.org/10.1016/j.ces.2007.08.047

Duocastella M, Sancataldo G, Saggau P et al (2017) Fast inertia-free volumetric light-sheet microscope. ACS Photonics 4(7):1797–1804. https://doi.org/10.1021/acsphotonics.7b00382

Elisa Z, Toon B, De Smedt SC et al (2018) Technical implementations of light sheet microscopy. Microsc Res Tech 81(9):941–958. https://doi.org/10.1002/jemt.22981

Filella A, Ern P, Roig V (2015) Oscillatory motion and wake of a bubble rising in a thin-gap cell. J Fluid Mech 778:60–88. https://doi.org/10.1017/jfm.2015.355

Fleckenstein S, Bothe D (2015) A Volume-of-Fluid-based numerical method for multi-component mass transfer with local volume changes. J Comput Phys 301:35–58. https://doi.org/10.1016/j.jcp.2015.08.011

Francois J, Dietrich N, Guiraud P et al (2011) Direct measurement of mass transfer around a single bubble by micro-PLIFI. Chem Eng Sci 66(14):3328–3338. https://doi.org/10.1016/j.ces.2011.01.049

Garcia-Ochoa F, Gomez E (2009) Bioreactor scale-up and oxygen transfer rate in microbial processes: an overview. Biotechnol Adv 27(2):153–176. https://doi.org/10.1016/j.biotechadv.2008.10.006

Greger K, Swoger J, Stelzer EHK (2007) Basic building units and properties of a fluorescence single plane illumination microscope. Rev Sci Instrum. https://doi.org/10.1063/1.2428277

Hofmann S, Weiland C, Fitschen J et al (2022) Lagrangian sensors in a stirred tank reactor: comparing trajectories from 4D-particle tracking velocimetry and Lattice-Boltzmann simulations. Chem Eng J 449:137549. https://doi.org/10.1016/j.cej.2022.137549

Huisken J, Swoger J, Del Bene F et al (2004) Optical sectioning deep inside live embryos by selective plane illumination microscopy. Science (New York NY) 305(5686):1007–1009. https://doi.org/10.1126/science.1100035

Jahl PE, Parthasarathy R (2020) Lipid bilayer hydrodynamic drag. Phys Rev Res 2(1):013132. https://doi.org/10.1103/PhysRevResearch.2.013132

Jimenez M, Dietrich N, Cockx A et al (2013) Experimental study of 2 diffusion coefficient measurement at a planar gas-liquid interface by planar laser-induced fluorescence with inhibition. AIChE J 59(1):325–333. https://doi.org/10.1002/aic.13805

Kameke AV, Kastens S, Rüttinger S et al (2019) How coherent structures dominate the residence time in a bubble wake: an experimental example. Chem Eng Sci 207:317–326. https://doi.org/10.1016/j.ces.2019.06.033

Kapoustina V, Guffart J, Hien A et al (2019) Influence of a single microstructure on local mass transfer in liquid film flows. Chem Eng Res Des 146:352–362. https://doi.org/10.1016/j.cherd.2019.04.022

Karnbach F, Yang X, Mutschke G et al (2016) Interplay of the open circuit potential-relaxation and the dissolution behavior of a single H2 bubble generated at a Pt microelectrode. J Phys Chem C 120(28):15137–15146. https://doi.org/10.1021/acs.jpcc.6b02305

Kexel F, von Kameke A, Tenhaus J et al (2021) Taylor bubble study of the influence of fluid dynamics on yield and selectivity in fast gas-liquid reactions. Chem Ing Tec 93(5):830–837. https://doi.org/10.1002/cite.202000241
Kováts PM (2021) Detailed experimental study of mass transfer and liquid flow in a bubble column with optical measurement techniques. PhD Thesis, https://repo.bibliothek.uni-halle.de/handle/1981185920/87195
Kursula L, Kexel F, Fitschen J et al (2022) Unsteady mass transfer in bubble wakes analyzed by Lagrangian coherent structures in a flat-bed reactor. Processes 10(12):2686. https://doi.org/10.3390/pr10122686
Kursula L, Kexel F, Hoffmann M et al (2026a) Data for publication: experimental studies on microscopic, multiphase transport phenomena: novel applications of light sheet fluorescence microscopy. https://doi.org/10.15480/882.15833
Kursula L, Kexel F, Hoffmann M et al (2026b) Supplementary information for publication: experimental studies on microscopic, multiphase transport phenomena: novel applications of light sheet fluorescence microscopy. https://doi.org/10.15480/882.16054
Lakowicz JR (2010) Principles of fluorescence spectroscopy, third edition, corrected at 4, printing. Springer, New York, NY
Lebrun G, Xu F, Le Men C et al (2021) Gas-liquid mass transfer around a rising bubble: combined effect of rheology and surfactant. Fluids 6(2):84. https://doi.org/10.3390/fluids6020084
Matthes S (2021) Fundamentals of microscale bubbles in process engineering, 1st edn. No. Band 9 in Berichte aus dem Institut für Mehrphasenströmungen, Cuvillier Verlag, Göttingen
Olarte OE, Andilla J, Gualda EJ et al (2018) Light-sheet microscopy: a tutorial. Adv Opt Photonics 10(1):111. https://doi.org/10.1364/AOP.10.000111
Pavlov L, Cazin S, Ern P et al (2021) Exploration by Shake-the-Box technique of the 3D perturbation induced by a bubble rising in a thin-gap cell. Exp Fluids 62(1):22. https://doi.org/10.1007/s00348-020-03117-z
Rehfeldt S, Stichlmair J (2007) Measurement and calculation of multicomponent diffusion coefficients in liquids. Fluid Phase Equilib 256(1):99–104. https://doi.org/10.1016/j.fluid.2006.10.008
Ritter JG, Veith R, Siebrasse JP et al (2008) High-contrast single-particle tracking by selective focal plane illumination microscopy. Opt Express 16(10):7142–7152. https://doi.org/10.1364/OE.16.007142
Roudet M, Billet AM, Cazin S et al (2017) Experimental investigation of interfacial mass transfer mechanisms for a confined high-reynolds-number bubble rising in a thin gap. AIChE J 63(6):2394–2408. https://doi.org/10.1002/aic.15562
Ruiz-Rus J, Ern P, Roig V et al (2022) Coalescence of bubbles in a high Reynolds number confined swarm. J Fluid Mech 944:A13. https://doi.org/10.1017/jfm.2022.492
Rüttinger S, Spille C, Hoffmann M et al (2018) Laser-induced fluorescence in multiphase systems. ChemBioEng Rev 5(4):253–269. https://doi.org/10.1002/cben.201800005
Schanz D, Gesemann S, Schröder A (2016) Shake-the-box: Lagrangian particle tracking at high particle image densities. Exp Fluids 57(5):70. https://doi.org/10.1007/s00348-016-2157-1
Schlüter M, Herres-Pawlis S, Nieken U et al (2021) Small-scale phenomena in reactive bubbly flows: experiments, numerical modeling, and applications. Annu Rev Chem Biomol Eng 12:625–643. https://doi.org/10.1146/annurev-chembioeng-092220-100517
Song X, Nobes DS (2011) Experimental investigation of evaporation-induced convection in water using laser based measurement techniques. Exp Thermal Fluid Sci 35(6):910–919. https://doi.org/10.1016/j.expthermflusci.2011.01.010
Stelzer EHK (2015) Light-sheet fluorescence microscopy for quantitative biology. Nat Methods 12(1):23–26. https://doi.org/10.1038/nmeth.3219
Stern O, Volmer M (1919) Über die Abklingungszeit der Fluoreszenz. Phys Z
Strobl F, Stelzer EHK (2014) Non-invasive long-term fluorescence live imaging of Tribolium castaneum embryos. Development 141(11):2331–2338. https://doi.org/10.1242/dev.108795
Taylor R, Krishna R (1993) Multicomponent mass transfer, Wiley series in chemical engineering. Wiley, New York
Timmermann J, Hoffmann M, Schlüter M (2016) Influence of bubble bouncing on mass transfer and chemical reaction. Chem Eng Technol 39(10):1955–1962. https://doi.org/10.1002/ceat.201600299
Tomančák P, Reynaud EG (2024) Let there be light sheet. Light sheet fluorescence microscopy. John Wiley & Sons Ltd, Hoboken, pp 1–10
Weiner A, Timmermann J, Pesci C et al (2019) Experimental and numerical investigation of reactive species transport around a small rising bubble. Chem Eng Sci X 1:100007. https://doi.org/10.1016/j.cesx.2019.100007
Xing W, Yin M, Lv Q et al (2014) 1 - Oxygen solubility, diffusion coefficient, and solution viscosity. In: Xing W, Yin G, Zhang J (eds) Rotating electrode methods and oxygen reduction electrocatalysts. Elsevier, Amsterdam, pp 1–31
Xu F, Hébrard G, Dietrich N (2020) Comparison of three different techniques for gas-liquid mass transfer visualization. Int J Heat Mass Transf 150:119261. https://doi.org/10.1016/j.ijheatmasstransfer.2019.119261